1

Molecular Dynamics Simulation of Shape-memory Behavior

Takuya Uehara
Yamagata Univ.
Japan

1. Introduction

Mechanical properties of shape-memory alloys (SMAs) are typically represented by the characteristic stress–strain curve, which forms a hysteresis loop in a loading, unloading and shape-recovering process. To represent the deformation behavior of SMAs, various constitutive equations have been developed, and prediction of the macroscopic behavior has been possible using finite-element simulations. The atomistic behavior leading to the deformation and shape-recovery is explained on the basis of the phase transformation between austenite and martensite phases and the characteristics of the crystal structure.

One well-known atomistic mechanism is illustrated in Fig. 1. The stable phase depends on the temperature, and phases at high and low temperature are body-centered cubic (bcc or B2) and martensite, respectively. The martensite phase consists of many *variants*, and each variant has a directional unit cell. In Fig. 1(b), for example, a unit cell of the martensite is illustrated as a box leaning in the positive or negative direction along the x-axis. Cells leaning in the same direction constitute a layer, and the direction of the lean alternates between layers. In this paper, the layer is called a variant, although a realistic variant is defined as a rather larger domain. The martensite phase is generated by cooling the B2 structure shown in Fig. 1(a). Randomly orientated variants are then generated, as shown in Fig. 1(b). When a shear load is imposed on this state, some of the layers change their orientation, as shown in Fig. 1(c). This structural change induces macroscopic deformation. When the external shear load is released, the strain does not return to the original state except for slight elastic recovery. When the specimen is heated to the transformation temperature, the martensite transforms into the B2 structure, and martensite appears again with cooling of the specimen. Since the B2 structure is cubic, the shape of the unit cell is independent of the orientation of the martensite layers. Therefore, the specimen macroscopically regains its original shape.

This mechanism is well known but has not been fully verified since direct observation of dynamic behavior in a wide range of temperatures is difficult. Therefore, computer simulation is expected to provide evidence for and further extend the mechanism. The molecular dynamics method has become a powerful and effective tool to investigate material properties and dynamic behavior on an atomistic scale, and it has also been applied in the case of SMAs. The stable structure of Ni_3Al, for instance, was investigated by Foiles and Daw (Foiles & Daw, 1987), Chen et al. (Chen et al., 1989) using an interatomic potential based on the embedded-atom method (EAM) with suitable parameters (Daw & Baskes, 1984; Foiles et al., 1986). The phase stability and transformation between B2 and martensite structures in NiAl was also

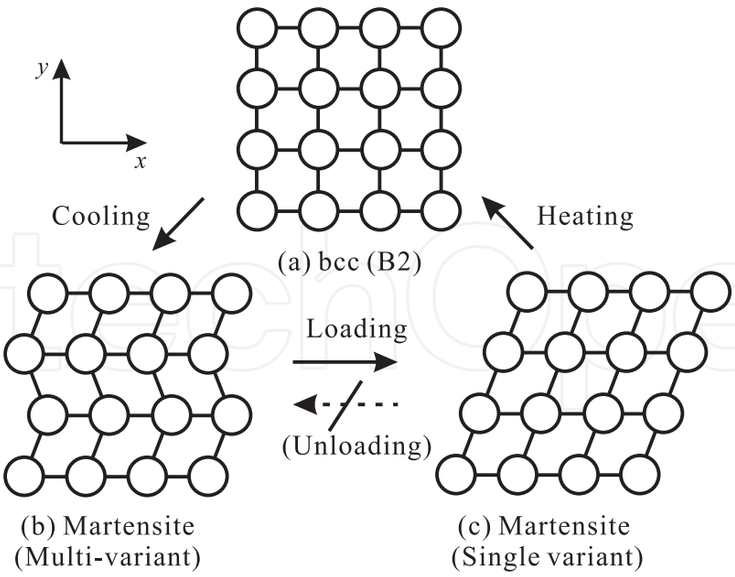

Fig. 1. Schematic illustration of deformation and shape recovery of a SMA.

reproduced using the EAM potential as reported by Rubini and Ballone (Rubini & Ballone, 1993) and Farkas et al. (Farkas et al., 1995). Uehara et al. then utilized the EAM potential to demonstrate the shape-memory behavior of Ni-Al alloy in terms of a small single crystal (Uehara et al., 2001; Uehara & Tamai, 2004, 2005, 2006), the size dependency (Uehara et al., 2006), and the polycrystalline model (Uehara et al., 2008, 2009). Ozgen and Adiguzel also investigated the shape-memory behavior of Ni-Al alloy using a Lennard-Jones (LJ) potential (Ozgen & Adiguzel, 2003, 2004). In addition, for Ni-Ti alloy, martensitic transformation was simulated by Sato et al. (Sato et al., 2004) and Ackland et al. (Ackland et al., 2008). It was also reported by Kastner (Kastner, 2003, 2006) that the shape-memory effect can be represented even by a two-dimensional model with a general LJ potential on the basis of thermodynamical discussion on the effect of temperature on the phase transformation. For a more practical purpose, Park et al. demonstrated shape-memory and pseudoelastic behavior during uniaxial loading of an fcc silver nanowire, and discussed the effect of the initial defects and mechanism of twin-boundary propagation (Park et al., 2005, 2006).

In this chapter, atomistic behavior and a stress–strain diagram obtained by molecular dynamics simulation are presented, following our simulation of Ni-Al alloy. A summary of the molecular dynamics method as well as EAM potential is given in Sec. 2. The simulation conditions are explained in Sec. 3. Simulation results obtained using the single-crystal model and polycrystal model are presented in Sec. 4 and 5, respectively, and concluding remarks are given in Sec. 6.

2. Molecular Dynamics Method

2.1 Fundamental equations

Employing the molecular dynamics (MD) method, the position and velocity of all atoms considered are traced by numerically solving Newton's equation of motion. Various physical and mechanical properties as well as dynamic behavior on the atomistic or crystal-structure scale are then obtained using a statistical procedure.

The fundamental equation of MD method is Newton's equation of motion for all atoms considered in the system:

$$\ddot{\mathbf{r}}_i = \mathbf{f}_i / m_i, \tag{1}$$

where $\mathbf{r}_i$ and m_i are the position vector and mass of the i-th atom, respectively, and $\mathbf{f}_i$ is the force acting on the i-th atom, which is represented as

$$\mathbf{f}_i = -\partial\Phi / \partial \mathbf{r}_i, \tag{2}$$

with the potential energy Φ of the system considered.
This equation is solved numerically. Verlet's scheme, which is often used in MD simulations, is utilized:

$$\mathbf{r}_i(t + \Delta t) = \mathbf{r}_i(t) + \mathbf{v}_i(t)\Delta t + \mathbf{F}_i(t)\Delta t^2 / (2m_i) \tag{3}$$

$$\mathbf{v}_i(t + \Delta t) = \mathbf{v}_i(t) + (\mathbf{F}_i(t + \Delta t) + \mathbf{F}_i(t))\Delta t / (2m_i), \tag{4}$$

where (t) represents the value at time t, and Δt is the time increment.
Temperature is expressed as

$$T = \frac{2K}{3Nk_b} = \frac{1}{3Nk_b} \sum_i^N m_i v_i^2, \tag{5}$$

where K is the total kinetic energy, k_b is the Boltzmann constant, and the notation $<>$ represents the time average. Temperature is controlled by scaling the velocity with the factor $\sqrt{T/T_0}$. Pressure is defined using the virial theorem, and it can be controlled by adjusting the length of the axes, which is referred to as the scaling method. The stress tensor is defined and controlled employing the so-called Parrinello-Rahman (PR) method (Parrinello & Rahman, 1980,1981).

2.2 EAM potential

Various interatomic energy functions have been proposed and are classified as empirical, semi-empirical, and first-principle potentials. The precision is highest for first-principle potentials, although only a small number of atoms are considered owing to the computational cost. This study employs the EAM potential, which was developed by Daw, Baskes (Daw & Baskes, 1984) and others, and the precision for metals is relatively fine. The potential function is written as

$$\Phi = \sum_i F(\rho_i) + \frac{1}{2} \sum_i \sum_{j \neq i} \phi_{ij}(r_{ij}). \tag{6}$$

Here, Φ is the total potential energy in the system considered, the first term on the right-hand side is a many-body term as a function of the local electron density ρ_i around the i-th atom, and the second term is a two-body term that expresses a repulsive force at close range.
The electron density ρ_i is assumed to be (Clementi & Roetti, 1974)

$$\rho_i = \sum_{j \neq i} \tilde{\rho}(r_{ij}) = \sum_{j \neq i} \{N^s \tilde{\rho}^s(r_{ij}) + N^d \tilde{\rho}^d(r_{ij})\}, \tag{7}$$

where

$$\tilde{\rho}^s(r_{ij}) = \tilde{\rho}^d(r_{ij}) = |\sum_I C_I R_I|^2 / 4\pi, \tag{8}$$

	Z_0	α	β	ν	N^{s}	N^{d}	k_1	k_2	k_3
Ni	10	1.554	0.352	0.5	1.7	8.3	-26.883	-34.040	-75.016
Al	3	1.3	1.5	0.5	0.76	2.24	-33.372	43.995	-186.75

Table 1. EAM parameters for Ni and Al in units of eV for energy and Å for length (I).

Ni				Al			
I	n_I	ζ_I	C_I	I	n_I	ζ_I	C_I
s 1	1	54.88885	-0.00389	s 1	1	26.89394	-0.00452
2	1	38.48431	-0.02991	2	1	20.27618	0.08395
3	2	27.42703	-0.03189	3	2	9.45860	-0.11622
4	2	20.88204	0.15289	4	2	6.86435	-0.18811
5	3	10.95707	-0.20048	5	3	3.35342	0.54265
6	3	7.31958	-0.05423	6	3	2.09388	0.55020
7	4	3.9265	0.49292	p 1	2	13.62535	-0.04475
8	4	2.15289	0.61875	2	2	6.90762	-0.14977
d 1	3	12.67582	0.4212	3	3	3.18100	0.26788
2	3	5.43253	0.70658	4	3	1.72743	0.80384

Table 2. EAM parameters (II).

and

$$R_I = \frac{(2\zeta_I)^{n_I+1/2}}{[(2n_I)!]^{1/2}} r_{ij}^{n_I-1} \exp(-\zeta_I r_{ij}). \tag{9}$$

Here, N^s, N^d, C_I, ζ_I, and n_I are parameters that depend on the species of the atom. These parameters are listed in a table by Clementi and Roetti for major metals, and the parameters for Ni and Al in this study are taken from the list; the parameters are given in Tables 1 and 2 in units of eV and Å.

The universal-function method proposed by Rose et al. (Rose et al., 1984) is applied to determine the embedding function F:

$$F(\rho) = k_1\rho^{1/2} + k_2\rho + k_3\rho^2, \tag{10}$$

where k_1, k_2, and k_3 are the parameters for Ni and Al, as given in Table 1.

The second term in Eq. (6) is a two-body term as a function of the distance between two atoms r_{ij}. The following form reported by Rubini and Ballone (Rubini & Ballone, 1993) is used.

$$\phi_{ij}(r_{ij}) = Z_i(r_{ij})Z_j(r_{ij})/r_{ij}\,, \tag{11}$$

$$Z(r_{ij}) = Z_0(1 + \beta r_{ij}^{\nu}) \exp(-\alpha r_{ij}). \tag{12}$$

Here Z_0, β, ν, and α are the parameters for Ni and Al; they are also listed in Table 1.

3. Model and Conditions

3.1 Simulation Model

Before demonstrating the shape-memory process, the stable structure of Ni-Al alloy ranging from 50% to 75% Ni at various temperatures is investigated using the aforementioned EAM

potential. The lattice points of B2 structure are assigned to Ni and Al atoms alternately to make Ni-50%Al alloy. An Al atom is then randomly chosen and replaced by a Ni atom. This procedure is repeated until the designated Ni concentration is reached. Using this model, MD simulations are carried out at a constant temperature under zero pressure with a periodic boundary condition.

Figure 2 presents the initial configuration of Ni and Al atoms and snapshots after a 20000-step calculation for (a) 60%Ni and (b) 68% Ni at 10 K. The crystal structure of the 68% model has apparently different, while no change is observed for the 60% model. The transformed phase is regarded as martensite. The stable structure is found to be B2 or martensite for all Ni concentrations and temperatures, as summarized in Fig. 3. Martensite phase is obtained at low temperature for the high-Ni alloy, while B2 is stable at high temperature in the low-Ni range. Since both structures are obtained in the 64%-70% range, the 68% Ni concentration is used in the following simulations.

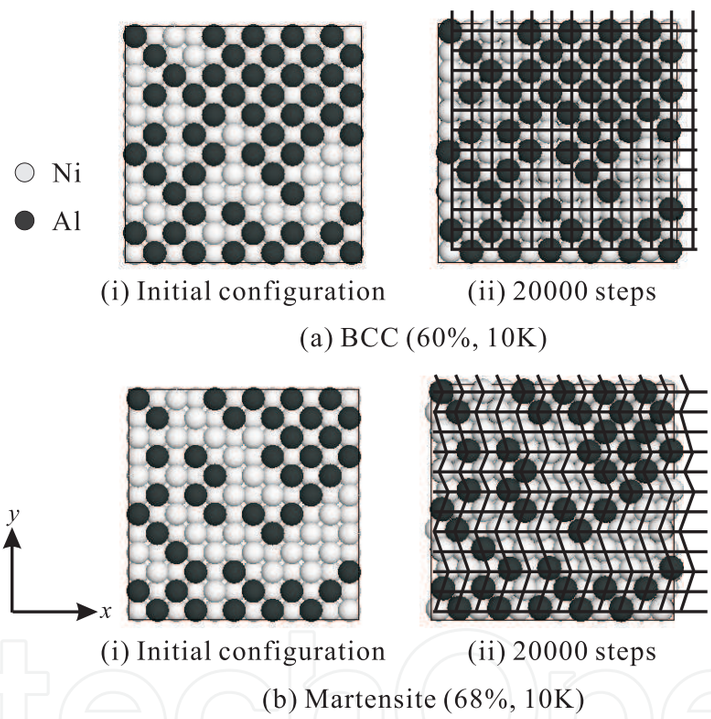

Fig. 2. Initial configuration of atoms and stable structures for (a) 60% Ni and (b) 68% Ni at 10 K.

3.2 Load and temperature condition

Figure 4 represents the external load and temperature profile divided into four stages: loading (I), unloading (II), heating (III) and cooling (IV). The time increment is set as Δt=1.5 fs, and the computation comprises 40000 steps. A shear load is imposed in the loading stage by leaning the edge that runs in the y direction in the x direction at a constant rate. The normal stress component is kept to zero by adjusting the three edge lengths. When the shear strain γ_{xy} reaches 0.33, the stress is released employing the Parrinello-Rahman (PR) method. This stage corresponds to the unloading. The temperature is kept constant at T=10 K through these

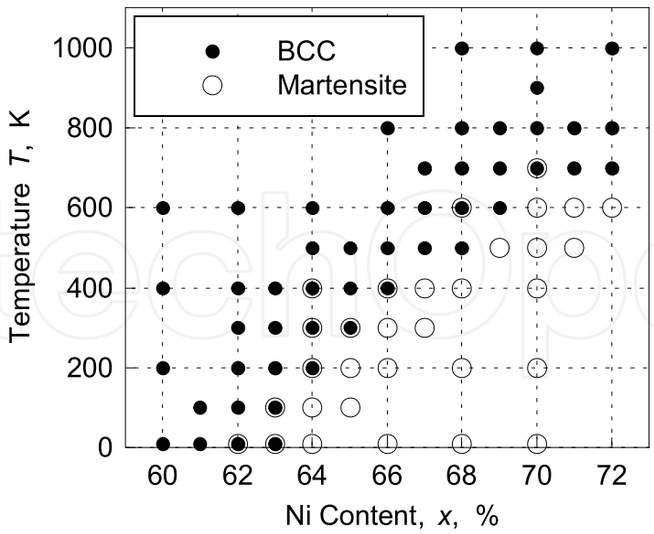

Fig. 3. Phase diagram representing stable structure.

stages, while it is raised to 1000 K and decreased to 10 K in Stages III and IV. Each component of the stress is controlled to zero through heat treatment employing the PR method.

4. Single-Crystal Model

4.1 Deformation and phase transformation

In this section, the results obtained using a single-crystal model with 68% Ni are presented following the work of Uehara et al. (Uehara et al., 2006a). The initial phase is set as martensite

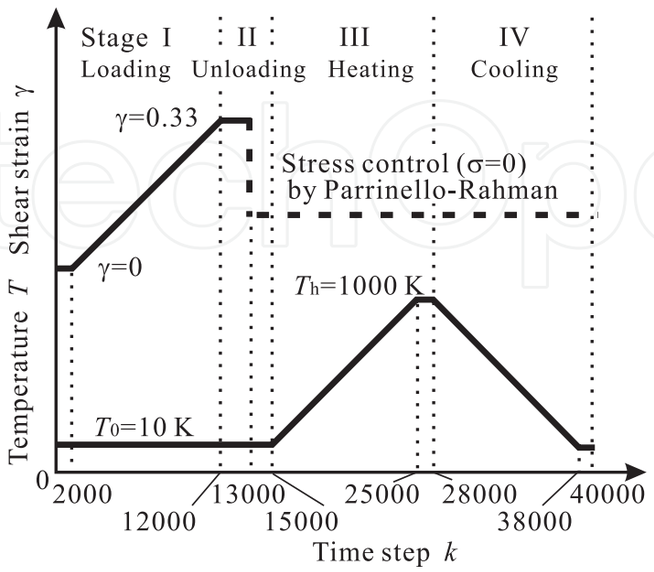

Fig. 4. Temperature and loading profile.

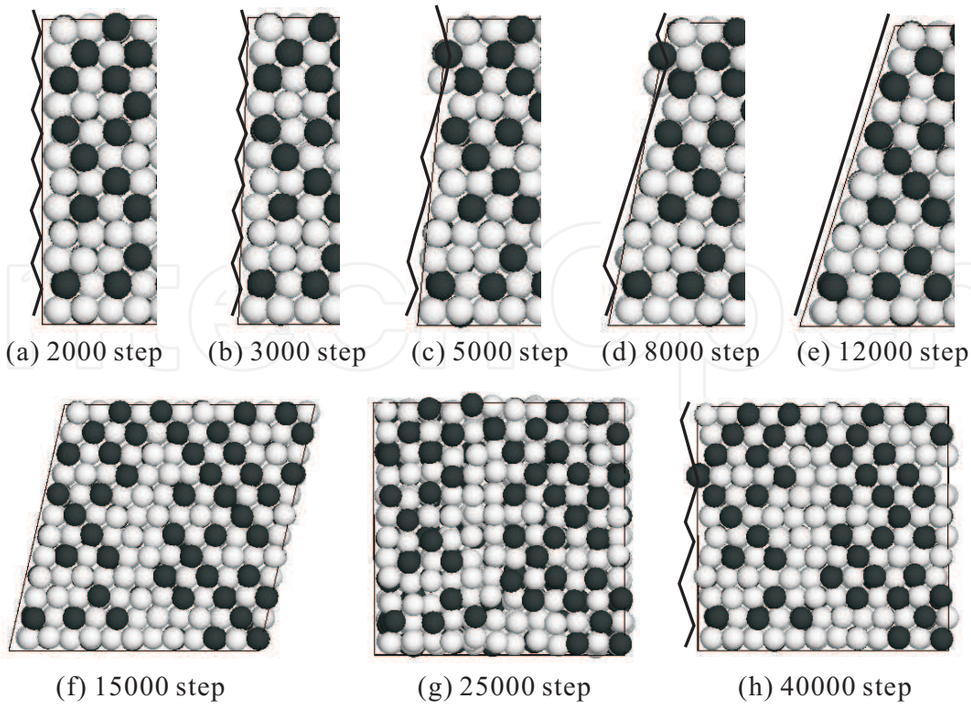

Fig. 5. Configuration of atoms during shear loading (a)–(e), after unloading (f), after heating (g), and in the final state (h).

comprising 864 atoms. Martensite phase in a variant has an lower angle in the $x - y$ plane and is arranged such that layers are parallel to the x-axis. Initially, 12 layers are stacked in the y-direction, and periodic boundary conditions are set in all directions.

Figure 5 represents the variation in the atomic configuration in the loading stage (a)-(e), after unloading (f), after heating (g), and after cooling (h). The Ni and Al atoms are depicted in gray and black, respectively, and auxiliary lines to clarify the variant stacking are drawn in the snapshots of the loading stage. When the shear strain is imposed, the model deforms elastically as shown in Fig. 5(b), in which the orientation of each layer does not change. Some layers change orientation by the 5000th step, and several consecutive layers become uniform, as shown in Fig. 5(c). This change in the layer direction occurs intermittently, and finally a single-variant martensite forms as shown in Fig. 5(e). The system is largely deformed on a macroscopic scale, and the distortion does not return to zero when the external force is released, as shown in Fig. 5(f), except for slight elastic recovery.

In the heating process, there is phase transformation from martensite to the B2 structure, and macroscopic deformation disappears, as shown in Fig. 5(g). Martensite again appears upon cooling. The variant layer is not identical to the initial state, although macroscopically, there is no change in shape, as shown in Fig. 5(h). Therefore, it is concluded that the deformation and shape recovery shown in Fig. 1 are well expressed by this model.

4.2 Stress–strain curve

The stress–strain (S-S) curve for the loading, unloading, heating, and cooling processes, corresponding to the atomistic behavior depicted in Fig. 5, is shown in Fig. 6. The loading curve consists of gradual rises and abrupt drops, and the lines as a whole is zigzag. Each of the

stress drops corresponds to the instant that a variant layer changes orientation, and this continues until all layers have the same orientation. The elastic recovery is clearly shown in this figure, and the shape recovery is expressed by the curve returning to the origin. As a result, the S-S curve draws a hysteresis loop, although the loading curve obtained experimentally or macroscopically is much smoother. Nevertheless, if neglecting the zigzag profile in loading, we conclude that the shape recovery is represented.

4.3 Size dependency

To show the size dependency, extensive simulations are carried out using larger models (Uehara et al., 2006b). The S-S curve obtained for a larger model is shown by the dashed line in Fig. 7(a), where the result for a smaller model identical to that in Fig. 6 is also drawn for comparison. The S-S curves have similar tendencies in the sense that there are repeated gradual stress rises and abrupt drops, although the number of peaks and drops is greater for the larger model; i.e., the curve as a whole is smoother for the larger model. The gradients of the two curves in the loading stage are identical, indicating that the elastic modulus is independent of the model size.

Random numbers are used in the preparation of the 68% Ni alloy, and to set the initial velocity of the atoms. Therefore, the results may be affected by the randomness. Figure 7(b) shows the S-S curves obtained in six trials, each of which had the same model size and conditions but different random-number set. The curves do not coincide completely, but mostly show identical tendencies.

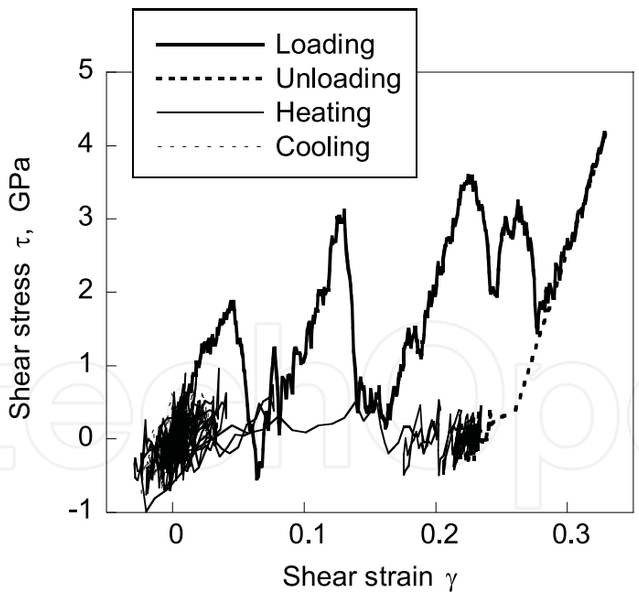

Fig. 6. Stress–strain relation during loading, unloading, heating, and cooling.

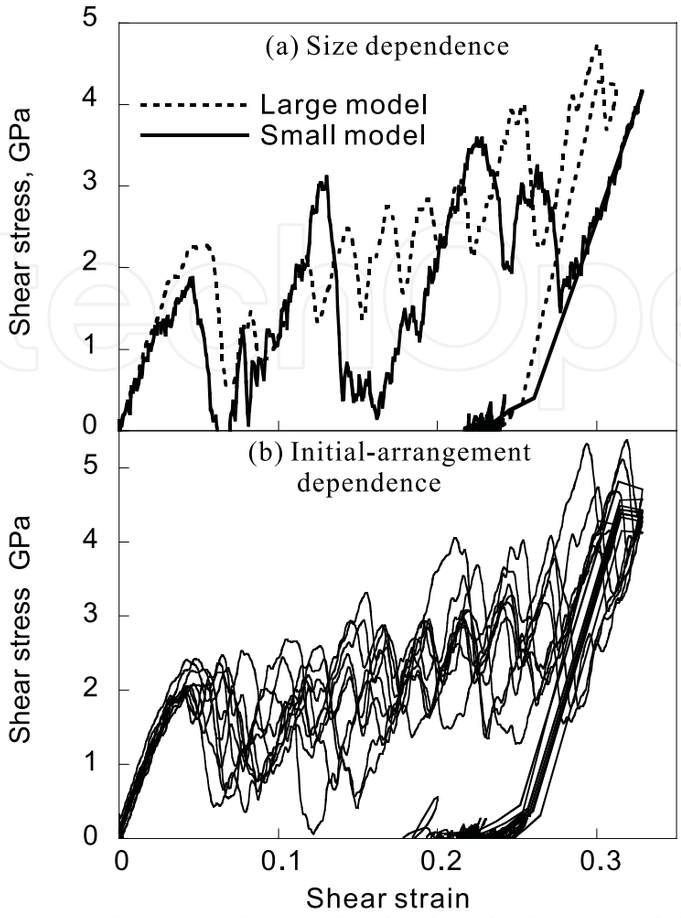

Fig. 7. Stress–strain curves during loading and unloading for larger models.

5. Polycrystalline Model

5.1 Model

Rather large discrepancy in the S-S curve, especially in the loading process, between the MD results and experimental observations is considered to be due to the MD model being highly simplified. To investigate to what degree the model affects the S-S curve, Uehara et al. carried out MD simulations using multi-grain models (Uehara et al., 2008, 2009), and the results are presented in this section.

Two models with different grain shapes and distributions are shown in Fig. 8. Model A consists of two square and two octagonal grains, while Model B has four hexagonal grains. Both models guarantee continuity under periodic boundary conditions. The initial configuration is set as martensite phase, while the orientations of the variants are specific to each grain. The model size is around $40\times40\times5$ in units of the lattice constant (i.e., about 16.6nm$\times$16.6nm$\times$1.5nm) in the x, y, and z directions, respectively, and the total number of atoms is about 31000. The conditions for shear loading and heat treatment are the same as those in the previous section.

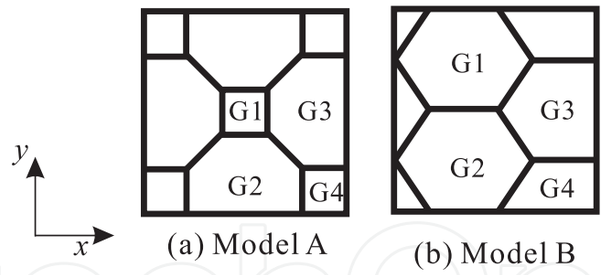

Fig. 8. Schematic illustration of the polycrystalline models.

5.2 Results for Model A

5.2.1 Configuration of atoms

Snapshots of the atomic configuration of Model A are shown in Fig. 9. The color indicates the local structure (Uehara et al., 2009), where M1 and M2 are the martensite phases consisting of variant layers with an alternating sequence and consecutive sequence, respectively.

The initial configuration and local structure are shown in Fig. 9(a). All atoms are arranged at the M1 martensite sites. In the preparation of the multi-grain model, large mismatches are introduced at the grain boundaries. Therefore, some relaxation behavior is observed in the initial stage, resulting in the appearance of B2 and M2 structures around the grain boundaries, as shown in Fig. 9(b). The overall shape of the model is also affected by the relaxation behavior, and slight leaning is observed. However, the changes are slight, and the non-deformed M1 structure remains. Accordingly, the loading simulation is continued after this relaxation stage. In the loading stage, the model is compulsively deformed; i.e., shear deformation in the x-y plane, as shown in Figs 9(c) and (d). In this stage, M1 atoms turn to M2 phase, and the ratio of M2 atoms increases as macroscopic deformation progresses. A characteristic feature of the M2 appearance is that layers having specific orientation form each grain. This process is mostly identical to that observed for the single-crystal model, but it is notable that the rate of growth of the M2 domain varies among grains, which is considered to be the major cause of the smoothing of the S-S curve as noted later. Finally, transformation from M1 to M2 is mostly complete by the end of loading, as shown in Fig. 9(d), while the grain boundaries (colored in green) remain at their initial positions. The macroscopic deformation disappears with release of the external force, as shown in Fig. 9(e). It is notable that the distribution of the local structure does not change in the unloading process.

In the following heat treatment process, the phase transformation from martensite to B2 occurs similarly to the single-crystal case, as shown in Fig. 9(f), and the macroscopic shape of the model regains its original shape. Note again that the grain boundaries are still distinguishable after B2 transformation. When the model has cooled, martensitic transformation occurs. Since the variants are generated with random orientations, the distribution of M1 and M2 differs from that of the initial state, but this is not critical here. There is in-depth discussion of the deformation mechanism in the literature (Uehara et al., 2009).

5.2.2 Stress–strain curve

Figure 10 represents the stress–strain relation throughout the loading, unloading, and heat treatment processes. The shear strain is added at a constant rate in the loading stage, and the corresponding time steps are shown on the upper side of the diagram. The S-S curve in Fig. 10 dramatically differs from those for single-crystal models shown in Figs. 6 and 7. The zigzag shape in the loading stage disappears and there is a smooth curve instead. The

sudden drop in stress is due to the simultaneous change in the orientation of a specific layer through the model in a single crystal. In the multi-grain model, however, the motion of the layer is interfered by the grain boundary, and the orientation change does not pass thorough the model. Therefore, there is no sudden drop in stress, and other layers begin to deform. This occurs continuously, resulting in the smoothing of the stress variation.
The subsequent elastic recovery in the unloading process — macroscopic shape recovery due to B2 transformation in the heating process — and regeneration of the original martensite phases are similar to what occurs for the single-crystal model, and a hysteresis loop forms. As a result, we conclude that the shape-memory behavior is successfully simulated, and the S-S curves using a multi-grain model approach the experimental curves.

5.3 Results for Model B

Figures 11 and 12 show the variation in the configuration of atoms and the S-S curves in the loading stage obtained using Model B. The snapshots in Figs. 11(a)–(d) correspond to the initial configuration, after relaxation, under loading, and at the end of loading, respectively. In Fig. 12, the S-S curves obtained in six cases, which differ in terms of the variant orientation in each grain, are plotted in a single diagram.
Similarly to what is seen in Fig. 9, there is some relaxation around the grain boundaries, and B2 and M2 domains appear as shown in Fig. 11(b). Here again, since the overall state of M1 phase is maintained, the loading process is continued using this model. The orientation of the martensite varies as the shear load is imposed, and the M2 domain grows. Each variant has a particular orientation within the grain, and finally, M2 occupies almost all grains except at grain boundaries. Note that in some cases, there are multiple orientations in a grain, which is also considered to be the cause of the smoothing of the S-S curve. In Fig. 12, the overall tendency is common for all trials, while the plateau stress is classified into two groups. Detailed discussion is provided in the literature (Uehara et al., 2009).

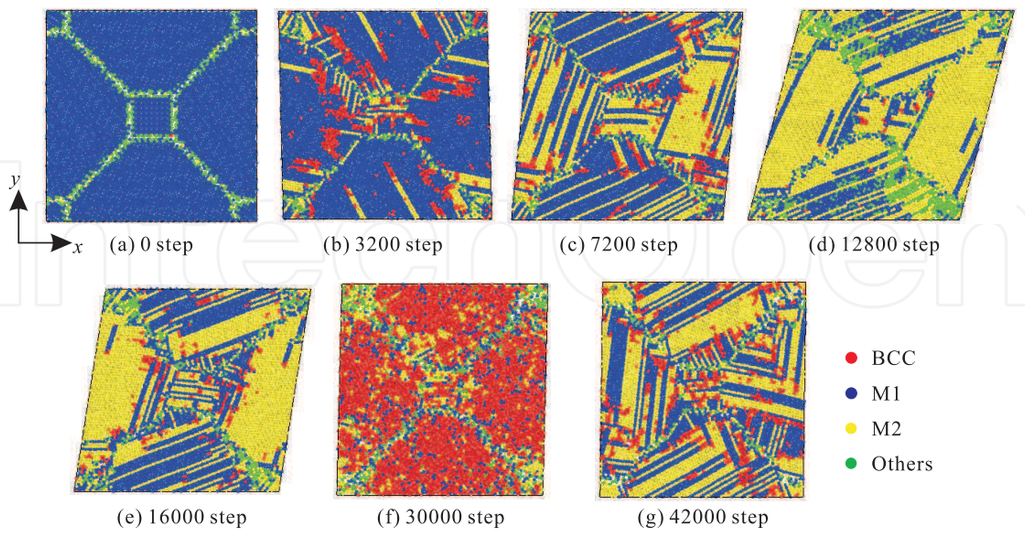

Fig. 9. Variation of the configuration of atoms for Model A: (a) initial state, (b) after relaxation, (c) under loading, (d) after loading, (e) after unloading, (f) after heating, and (g) after cooling.

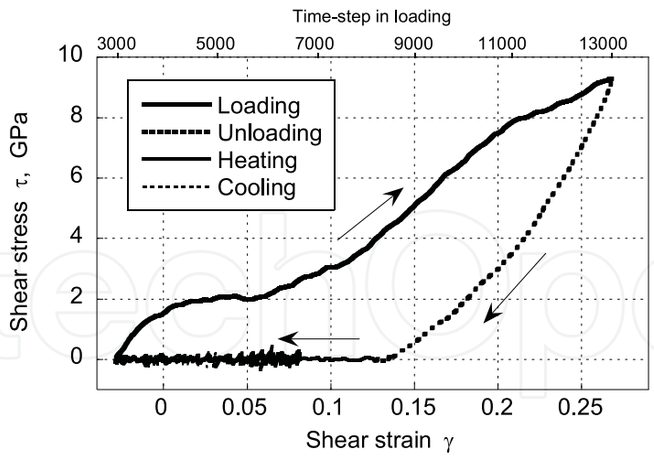

Fig. 10. Stress–strain relation during loading, unloading, heating, and cooling for Model A.

6. Concluding Remarks

Deformation and shape-recovery processes are simulated employing the molecular dynamics method. There is shape memory even in a simple model of a single crystal, and a hysteresis loop for the stress–strain curve is obtained. Deformation of martensite phase progresses through layer-by-layer change in the variant orientation, and the propagation results in a zigzag shape of the S-S curve. The shape of the loading curve drastically changes when using a multi-grain model, and the S-S curve approaches the experimentally observed curve, which is obtained on a macroscopic scale. It is revealed in this study that the smoothing of the curve is due to the existence of grain boundaries and variation in the crystal orientation.
As future work, extensive simulations are required for detailed discussion on the role of the grain boundary and anisotropic tendency. Other effects and mechanisms based on defects, dislocations, sliding, and twinning, which are especially important in SMAs, should be considered. The size dependency is also expected to be investigated in depth in terms of the above-mentioned mechanism, since it is one of the major remaining problems in solid mechanics (Yamakov et al., 2002; Shimokawa et al., 2005). For quantitative evaluation, the precision of the interatomic potential should be definitive and a three-dimensional model used.

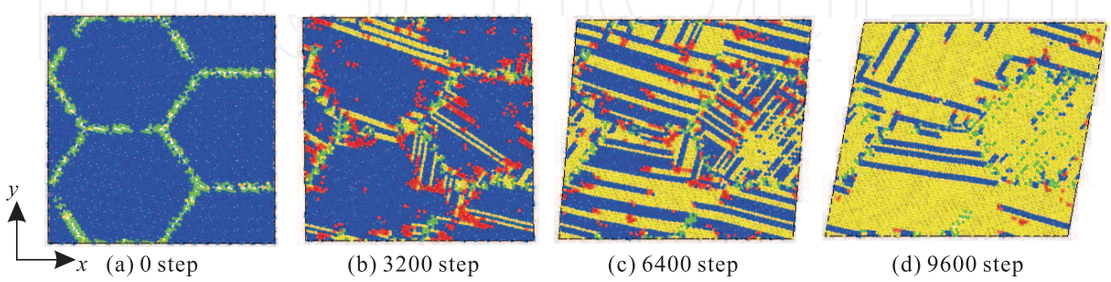

Fig. 11. Variation of the configuration of atoms for Model B: (a) initial state, (b) after relaxation, (c) under loading, and (d) after loading.

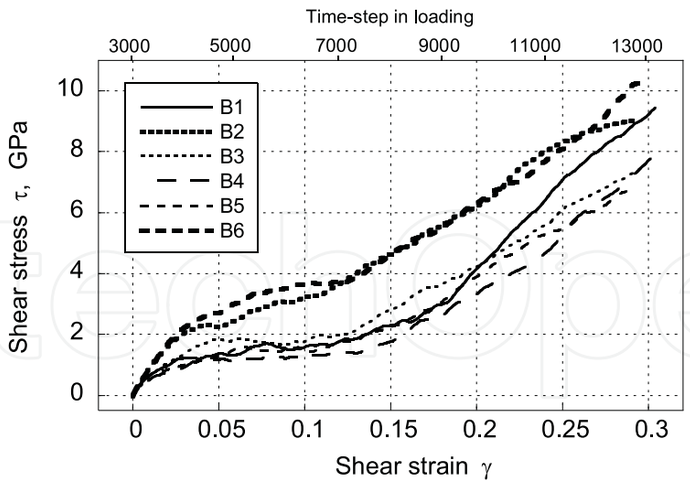

Fig. 12. Stress–strain relation in the loading stage using Model B with different sets of variant orientations in the grains.

Nevertheless, it is concluded that the molecular dynamics simulation is a powerful and promising tool for clarifying the mechanism of the shape-memory behavior and will allow prediction of new functionalities and further development of advanced devices.

7. References

Ackland, G. J.; Jones, A. P. & Noble-Eddy, R. (2008). Molecular dynamics simulations of the martensitic phase transition process. *Mater. Sci. Eng. A*, Vol. 481-482, 11-17.

Chen, S. P.; Srolovitz, D. J. & Voter, A. F. (1989). Computer simulation on surfaces and [001] symmetric tilt grain boundaries in Ni, Al, and Ni_3Al. *J. Mater. Res.*, Vol. 4, 62-77.

Clapp, P. C.; Rifkin, J.; Kenyon, J. & Tanner, L. E. (1988). Computer study of tweed as a precursor to a martensitic transformation of a bcc lattice. *Metall. Trans. A*, Vol. 19, 783-787.

Clementi, E. & Roetti, C. (1974). Roothaan-Hartree-Fock atomic wavefunctions. *Atomic Data and Nuclear Data Tables*, Vol. 14, 177-478.

Daw, M. S. & Baskes, M. I. (1984). Embedded-atom method: Derivation and application to impurities, surfaces, and other defects in metals. *Phys. Rev. B*, Vol. 29, 6443-6463.

Elliott, R. S.; Shaw, J. A. & Triantafyllidis, N. (2002). Stability of thermally-induced martensitic transformations in bi-atomic crystals. *J. Mech. Phys. Solids*, Vol. 50, 2463-2493.

Elliott, R. S.; Shaw, J. A. & Triantafyllidis, N. (2006). Stability of crystalline solids — II: Application to temperature-induced martensitic phase. *J. Mech. Phys. Solids*, Vol. 54, 193-232.

Farkas, D; Mutasa, B.; Vailhe, C. & Ternes, K. (1995). Interatomic potentials for B2 NiAl and martensitic phases. *Modelling Simul. Mater. Sci. Eng.*, Vol. 3, 201-214.

Foiles, S. M.; Baskes, M. I. & Daw, M. S. (1986). Embedded-atom-method functions for the fcc metals Cu, Ag, Au, Ni, Pd, Pt, and their alloys. *Phys. Rev. B*, Vol. 33, 7983-7991.

Foiles, S. M. & Daw, M. S. (1987). Application of the embedded atom method of Ni_3Al. *J. Mater. Res.*, Vol. 2, 5-15.

Huang, X.; Ackland, G. J. & Rabe, K. M. (2003). Crystal structures and shape-memory behaviour of NiTi. *Nature Mater.*, Vol. 2, 307-311.

Ji, C. & Park, H. S. (2007). The effect of defects on the mechanical behavior of silver shape memory nanowires. *J. Comput. Theor. Nanosci.*, Vol. 4, 578-587.

Kastner, O. (2003). Molecular-dynamics of a 2D model of the shape memory effect Part I: Model and simulations. *Continuum Mech. Thermodyn.*, Vol. 15, 487-502.

Kastner, O. (2006). Molecular-dynamics of a 2D model of the shape memory effect Part II: thermodynamics of a small system. *Continuum Mech. Thermodyn.*, Vol. 18, 63-81.

Leo, P. H.; Shield, T. W. & Bruno, O. P. (1993). Transient heat transfer effects on the pseudoelastic behavior of shape-memory wires. *Acta Metall. Mater.*, Vol. 41, 2477-2485.

Ozgen, S. & Adiguzel, O. (2003). Molecular dynamics simulation of diffusionless phase transformation in a quenched NiAl alloy model. *J. Phys. Chem. Solids*, Vol. 64, 459-464.

Ozgen, S. & Adiguzel, O. (2004). Investigation of the thermoelastic phase transformation in a NiAl alloy by molecular dynamics simulation. *J. Phys. Chem. Solids*, Vol. 65, 861-865.

Park, H. S.; Gall, K. & Zimmerman, J. A. (2005). Shape memory and pseudoelasticity in metal nanowires. *Phys. Rev. Lett.*, Vol. 95, 255504.

Park, H. S. & Ji, C. (2006). On the thermomechanical deformation of silver shape memory nanowires. *Acta Mater.*, Vol. 54, 2645-2654.

Parrinello, M. & Rahman, A. (1980). Crystal structure and pair potentials: A molecular-dynamics study. *Phys. Rev. Lett.*, Vol. 45, 1196-1199.

Parrinello, M. & Rahman, A. (1981). Polymorphic transitions in single crystals: A new molecular dynamics method. *J. Appl. Phys.*, Vol. 52, 7182-7190.

Rose, J. H.; Smith, J. R.; Huina, J. & Ferrante, J. (1984). Universal features of the equation of state of metals. *Phys. Rev. B*, Vol. 29, 2963-2969.

Rubini, S. & Ballone, P. (1993). Quasiharmonic and molecular-dynamics study of the martensitic transformation in Ni-Al alloys. *Phys. Rev. B*, Vol. 48, 99-111.

Sato, T.; Saito, K.; Uehara, T. & Shinke, N. (2004). Molecular dynamics study on nano structure and shape-memory property of Ni-Ti alloy. *Trans. Mat. Res. Soc. Japan*, Vol. 29, 3615-3618.

Sato, T.; Saitoh, K. & Shinke, N. (2006). Molecular dynamics study on microscopic mechanism for phase transformation of Ni-Ti alloy. *Modelling Simul. Mater. Sci. Eng.*, Vol. 14, S39-S46.

Shao, Y.; Clapp, P. C. & Rifkin, J. A. (1996). Molecular dynamics simulation of martensitic transformations in NiAl. *Metall. Mater. Trans. A*, Vol. 27, 1477-1489.

Shimokawa, T.; Kinari, T.; Shintaku, S.; Nakatani, A. & Kitagawa, H. (2005). Defect-induced anisotropy in mechanical properties of nanocrystalline metals by molecular dynamics simulations. *Modelling Simul. Mater. Sci. Eng.*, Vol. 13, 1217-1231.

Uehara, T.; Masago, N. & Inoue, T. (2001). An atomistic study on temperature-incorporated phase transformation in Ni-Al alloy. *Proc. 50th JSMS Annual Meet.*, 283-284.

Uehara, T. & Tamai, T. (2004). Molecular dynamics simulations on shape memory effect in Ni-Al alloy. *Proc. 6th World Cong. Comp. Mech.*, CD-ROM.

Uehara, T. & Tamai, T. (2005). Molecular dynamics simulation on shape-memory effect in Ni-Al alloy by using EAM potential. *Trans. Japan Soc. Mech. Eng.*, Vol. 71, No. 705, 717-723. (in Japanese)

Uehara, T. & Tamai, T. (2006a). An atomistic study on shape-memory effect by shear deformation and phase transformation. *Mechanics of Advanced Materials and Structures*, Vol. 13, 197-204.

Uehara, T.; Tamai, T. & Ohno, N. (2006b). Molecular dynamics simulations of the shape-memory behavior based on martensite transformation and shear deformation. *JSME Int. J. A*, Vol. 49, 300-306.

Uehara, T.; Asai, C. & Ohno, N. (2008). Molecular dynamics simulations on the eeformation mechanism of multi-grain shape-memory alloy. *Advances in Heterogeneous Material Mechanics*, Eds. Fan, J. & Chen, H., 316-319.

Uehara, T.; Asai, C. & Ohno, N. (2009). Molecular dynamics simulations of the shape memory behavior using a multi-grain model. *Modelling Simul. Mater. Sci. Eng.*, Vol. 17, 035011.

Wagner, M. F. X. & Windl, W. (2008). Lattice stability, elastic constants and macroscopic moduli of NiTi martensites from first principles. *Acta Mater.*, Vol. 56, 6232-6245.

Yamakov, V.; Wolf, D.; Phillpot, S. R. & Gleiter, H. (2002). Deformation twinning in nanocrystalline Al by molecular-dynamics simulation. *Acta Materialia*, Vol. 50, 5005-5020.

IntechOpen

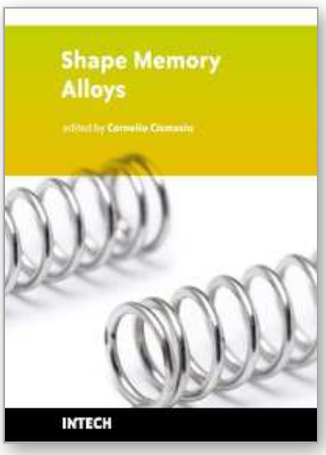

Shape Memory Alloys

Edited by Corneliu Cismasiu

ISBN 978-953-307-106-0

Hard cover, 210 pages

Publisher Sciyo

Published online 18, October, 2010

Published in print edition October, 2010

In the last decades, the Shape Memory Alloys, with their peculiar thermo-mechanical properties, high corrosion and extraordinary fatigue resistance, have become more popular in research and engineering applications. This book contains a number of relevant international contributions related to their properties, constitutive models and numerical simulation, medical and civil engineering applications, as well as aspects related to their processing.

How to reference

In order to correctly reference this scholarly work, feel free to copy and paste the following:

Takuya Uehara (2010). Molecular Dynamics Simulation of Shape-Memory Behavior, Shape Memory Alloys, Corneliu Cismasiu (Ed.), ISBN: 978-953-307-106-0, InTech, Available from: http://www.intechopen.com/books/shape-memory-alloys/molecular-dynamics-simulation-of-shape-memory-behavior

INTECH
open science | open minds

InTech Europe
University Campus STeP Ri
Slavka Krautzeka 83/A
51000 Rijeka, Croatia
Phone: +385 (51) 770 447
Fax: +385 (51) 686 166
www.intechopen.com

InTech China
Unit 405, Office Block, Hotel Equatorial Shanghai
No.65, Yan An Road (West), Shanghai, 200040, China
中国上海市延安西路65号上海国际贵都大饭店办公楼405单元
Phone: +86-21-62489820
Fax: +86-21-62489821

IntechOpen